# Interaction of acoustic and optical phonons in a soft-bonded Cu-Se framework of large unit cell minerals with anionic disorders

Kewal Singh Rana,[1] Raveena Gupta,[2] Debattam Sarkar,[3] Niraj Kumar Singh,[1] Somnath Acharya,[4] Satish Vitta,[4] Chandan Bera,[2] Kanishka Biswas,[3] and Ajay Soni[1,*]

[1]*School of Physical Sciences, Indian Institute of Technology Mandi, Mandi 175075, Himachal Pradesh, India*
[2]*Institute of Nano Science and Technology, Knowledge City, Sahibzada Ajit Singh Nagar, 140306 Punjab, India*
[3]*New Chemistry Unit, School of Advanced Materials and International Centre of Materials Science, Jawaharlal Nehru Centre for Advanced Scientific Research (JNCASR), Jakkur, Bangalore 560064, India*
[4]*Department of Metallurgical Engineering and Materials Science, Indian Institute of Technology Bombay, Mumbai 400076, India*

(Received 22 April 2023; revised 25 June 2023; accepted 28 June 2023; published 19 July 2023)

In general, optical and acoustic phonons have different energy scaling and are separated by an energy gap. However, the two phonon branches can also interact and provide an inherently poor thermal conductivity in complex minerals with a large number of atoms per unit cell. For instance, the copper-chalcogenide based minerals with high crystalline anharmonicity are inherently poor thermal conductors. We have studied large unit cell $Cu_{26}Nb_2Sn_6Se_{32}$, $Cu_{26}Nb_2Sn_6Se_{31.5}$, and $Cu_{26}Nb_2Sn_6Se_{30}Te_2$ synthetic minerals with a strategically tailored anionic disorder. These compounds have a *p*-type degenerate behavior with carrier concentration ($\sim$2.7–$\sim$15.3) $\times 10^{20}$ cm$^{-3}$, at 300 K and a very low lattice thermal conductivity, ($\sim$0.76–$\sim$1.49) W m$^{-1}$ K$^{-1}$ at $\sim$625 K. Here, the softening of Cu-Se bonds and hence the crystal framework play an important role for very poor thermal conductivity. The existence of two low frequency Raman active optical modes (at $\sim$55 and 72 cm$^{-1}$) associated with soft Cu and Se atoms, three localized Einstein modes in specific heat, suggest a high scattering of acoustic and optical branches with very short phonon lifetime ($\sim$0.3–0.6 ps). The excess vibrational density of states at low energies with compressed and flat optical branches strongly hinders the heat transport. The involvement of the Te atom at Se sites results in a lowering of the acoustic phonon cutoff frequency and the softening of optical phonons, significantly. Overall, $Cu_{26}Nb_2Sn_6Se_{30}Te_2$ has the lowest thermal conductivity at $\sim$625 K and is a promising thermoelectric material because of robust acoustic-optical phonon scattering, very low sound velocity, and high crystalline anharmonicity.

DOI: 10.1103/PhysRevB.108.045202

## I. INTRODUCTION

The fundamental understanding of the heat transport inside the complex crystal structure materials is crucial because the thermal energy is carried by both phonons as well as free charge carriers inside the crystalline material [1]. In recent times, minerals have been studied extensively due to their intrinsic properties of ultralow lattice thermal conductivity ($\kappa_l$). While the free charge carriers are crucial for both good electrical conductivity and electronic thermal conductivity ($\kappa_e$), the phonons primarily contribute to the $\kappa_l$. Thus, higher phonon scattering is an essential requirement for poor $\kappa_l$, which can give better thermal management in electronic devices and thermoelectric (TE) technology [1]. For this, the charge and heat carriers have to be decoupled to tune them separately. The minimization of heat transport in a material can be achieved via alloying [2], nanostructuring [3], soft-phonon modes [4], nanoscale defects [5], atomic rattlers [6], large unit cell [7], superionic materials [8,9], and strong crystal anharmonicity [10,11]. Based on the vibrations of the involved atoms, the acoustic and optical phonon branches have a different energy scaling with a forbidden energy gap [12]. However, in complex structure materials, the strong interaction between acoustic and optical phonons in the low frequency regime can lead to an inherently poor $\kappa_l$ [13–15].

The chalcogen family of compounds (S, Se, and Te) have shown the greatest impact in many advanced technologies in light and thermal energy harvesting [16–18]. Various binary, ternary, and quaternary copper chalcogenides and their derivatives with transition elements (Fe, Mn, Zn, Co, Nb, V, Ni) have very low $\kappa_l$ and can be considered as potential thermal energy harvesting materials [16]. Especially for TE research, materials such as colusites, $Cu_{26}A_2B_6S_{32}$ ($A$ = Nb, V, Mo, W, Cr, Ta; $B$ = Ge, As, Sn) [19–23], chalcopyrites, Cu(Ga, In)$Te_2$ [24], tetrahedrites, $Cu_{12-x}M_x(Sb, As)_4S_{13}$ ($M$ = Mn, Fe, Co, Ni, Cu, and Zn) [25–28], argyrodites, $A^{m+}_{(12-n)/m}M^{n+}X_6^{-2}$ ($A$ = Ag, Cu; $M$ = Si, Sn, Ge, Ga; $X$ = S, Se, Te) [9,29], superionic $MCrX_2$ ($M$ = Ag, Cu; $X$ = S, Se) [30], sulfide bornite, $Cu_5FeS_4$ [31], kuramite, $Cu_3SnS_4$ [32], and kesterite, $Cu_2(Cd, Zn)Sn(S, Se)_4$ [33,34] show low $\kappa_l$ due to complexity in the crystal structure [16]. The major reasons are large unit cells with crystalline anharmonicity, excessive vibrational density of states, and poor sound velocity, which result in enhanced phonon scattering and inherently low $\kappa_l$ in these materials [4,29,35,36].

Colusites are such types of materials which have a simple cubic crystal structure having large number of atoms per unit

*Author to whom correspondence should be addressed: ajay@iitmandi.ac.in

 

cell, high electronic transport, and poor thermal transport due to structural complexity [15,20,37]. In colusites, high electrical transport can be tuned with strong hybridization between the transition (Cu-3$d$) and chalcogen (S-3$p$) orbitals [19,38]. Here, the presence of unoccupied states above the Fermi level ($E_F$) results in a $p$-type semiconductor; the electron-deficient character can also be counted by the valency of $Cu^+$ ($Z = 29,\ 3d^{10}$), $Nb^{5+}$ ($Z = 41,\ 3d^0$), $Sn^{4+}$($Z = 50,\ 4d^{10}$), and $S^{2-}$ ($Z = 16,\ 3p^6$) ions [39]. Most of the available literature on colusites focuses on chemical tailoring at the cationic sites keeping sulfur as the anion [38,40,41]. It is observed that sulfur sublimation can induce large atomic scale defects, antisite defects, and interstitial defects which can result in strong phonon scattering and poor $\kappa_l$. [19,20,42,43].

In this study, we investigated the origin of poor thermal transport in synthetic minerals, $Cu_{26}Nb_2Sn_6Se_{32}$ (CNS-$Se_{32}$), $Cu_{26}Nb_2Sn_6Se_{31.5}$ (CNS-$Se_{31.5}$), and $Cu_{26}Nb_2Sn_6Se_{30}Te_2$ (CNS-$Se_{30}Te_2$). A significant reduction in $\kappa_l$ is observed from CNS-$Se_{32}$ to CNS-$Se_{30}Te_2$ at high temperatures. The low values of $\kappa_l$ in CNS-$Se_{30}Te_2$ is due to large anharmonicity and high phonon scattering from point defects and anion site disorders. The excess phonon density of states results in a boson peak at low temperature as investigated by heat capacity analysis. Further, the local Einstein modes interact with the low energy optical modes, suggest multiphonon scattering in the material system. The large number of atoms in the primitive cell results in the shrinkage of the first Brillouin zone, which leads to folded of high frequency vibrational modes as compressed optical modes with significant reduction in the velocities (flat bands) near zone boundaries [44]. The experimental work is supported by first principle calculations on electronic band structure and phonon dispersion, which also confirms the involvements of Cu and Se atoms and associated phonon modes for low $\kappa_l$. The heavier Te atom results in enhanced crystalline anharmonicity by lowering the acoustic phonon cutoff frequency and softening of optical phonons. Overall, we developed the connection between the nature of chemical bonding and transportation of heat carrying phonons inside the complex crystal structure minerals of crystalline solids.

## II. EXPERIMENTAL DETAILS

Polycrystalline samples of CNS-$Se_{32}$, CNS-$Se_{31.5}$, and CNS-$Se_{30}Te_2$ were synthesized in the laboratory via the solid state melt-grown technique [8,10]. High purity (∼99.99%) elemental Cu, Nb, Sn, Se, and Te were weighed in stoichiometric ratio and placed in quartz tubes of ∼10 mm diameter, and the tubes were flame-sealed at a vacuum of $\sim 10^{-5}$ mbar. The sealed tubes were heated to ∼1320 K with a rate of ∼0.3 K $min^{-1}$ and kept at ∼1320 K temperature for ∼48 h. Later, the tubes were cooled down to ∼670 K with a rate of ∼0.6 K $min^{-1}$, followed by further cooling to room temperature with a rate of ∼1 K $min^{-1}$. The obtained ingots were ground and subjected to hot-pressing at 720 K under a uniaxial pressure of 30 MPa in Ar atmosphere for a period of ∼1 h to get the pellets for transport measurements. Mass density ($d_m$) of the obtained hot-pressed pellets was found to be ∼5.7 g $cm^{-3}$ for CNS-$Se_{32}$ and CNS-$Se_{31.5}$; ∼5.6 g $cm^{-3}$ for CNS-$Se_{30}Te_2$, as assessed via the Archimedes principle. Crystal structure and phase purity study were identified by x-ray diffraction using a Rigaku Smart lab rotating anode diffractometer through Cu$K_\alpha$ as the radiation source ($\lambda \sim 1.5406$ Å) with the scan rate of 2° $min^{-1}$ and step size of 0.02°. The Hall measurements and low temperature heat capacity ($C_p$) were performed using physical property measurement system (PPMS, Quantum Design). The high temperature (320–640 K), resistivity ($\rho$), and Seebeck coefficient ($S$) measurements were performed using a ZEM-3 ULVAC instrument on bar-shaped pellets. Further, the total thermal conductivity ($\kappa_{\text{total}}$) was calculated using the relation $\kappa_{\text{total}} = DC_pd_m$ (where $D$ and $C_p$ are the thermal diffusivity and specific heat, respectively, and are estimated by using a NETZSCH-Laser flash apparatus and Dulong-Petit limit) [20,45]. The $\kappa_{\text{total}}$ was the sum of electrical ($\kappa_e$) and lattice ($\kappa_l$) parts of the thermal conductivity, where $\kappa_l = \kappa_{\text{total}}–(LT/\rho)$, where $\rho$, $L$, and $T$ are the electrical resistivity, Lorenz number, and absolute temperature, respectively. Field emission scanning electron microscope (FE-SEM) and energy dispersive x-ray spectroscopy of the polished pellets were examined from JFEI, USA, make Nova Nano SEM-450. High resolution transmission electron microscopy (HR-TEM) was performed through a FEI Tecnai G2 20S-twin microscope operating at 200 kV under vacuum conditions. The Raman spectroscopic measurements were carried out using a Jobin-Yvon Horiba LabRAM HR evolution Raman spectrometer, where a 532-nm excitation laser was used to excite the samples and Raman spectra were recorded with 1800 grooves/mm grating and an ultralow frequency filter was used for eliminating the Rayleigh line to access low frequency Raman modes. A Linkam stage was used for high temperature dependent (300–500 K) Raman studies. Furthermore, the details of the Rietveld refinement, elemental distribution of mapping, structural details, Raman spectroscopy, and thermal transport analysis can be found in the Supplemental Material [46].

## III. COMPUTATIONAL DETAILS

The electronic structures were investigated using density functional theory within the Vienna Ab initio Simulation Package (VASP) framework [47,48]. The projector-augmented-wave method [47,49], combined with the Perdew-Burke-Ernzerhof [50] approximation for the exchange and correlation terms of the functional, was employed. A plane-wave cutoff of 400 eV was set, and the structures were relaxed using a 4 × 4 × 1 Monkhorst-Pack grid for integrations over the Brillouin zone. A tolerance of $10^{-8}$ eV was established for the total energy and band energies, and calculations were continued until the absolute value of all components of the force was lower than 0.01 eV $Å^{-1}$. To determine the phonon band structure, a real-space approach was utilized to extract the force constants, as implemented in the PHONOPY package [51]. For calculating the interatomic force constants, 2 × 2 × 1 supercells and displacements with an amplitude of 0.01 Å were used, and forces were computed with VASP.

## IV. X-RAY DIFFRACTION AND MICROSTRUCTURAL ANALYSIS

X-ray diffraction (XRD) patterns of finely ground powders of hot-pressed CNS-$Se_{32}$, CNS-$Se_{31.5}$, and CNS-$Se_{30}Te_2$

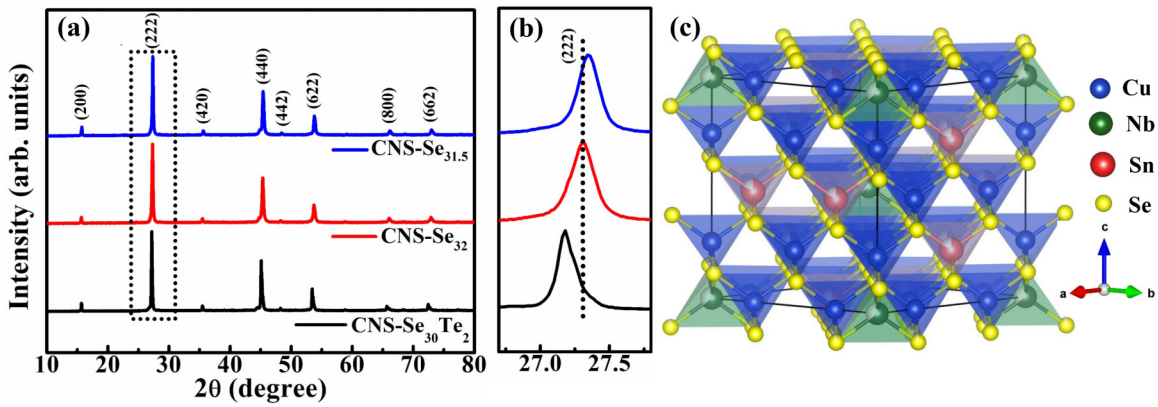


FIG. 1. (a) Powder XRD pattern of CNS-$Se_{32}$, CNS-$Se_{31.5}$, and CNS-$Se_{30}Te_2$, (b) enlarged 222 peak showing lattice expansion of CNS-$Se_{30}Te_2$ and contraction of CNS-$Se_{31.5}$ with respect to CNS-$Se_{32}$, and (c) cubic crystal structure of CNS-$Se_{32}$.

[Fig. 1(a)] show the crystalline nature and phase purity of the prepared samples. All these compounds crystallize into cubic crystal structure with space group $P\bar{4}3n$ [19]. The Rietveld refinement of CNS-$Se_{32}$, CNS-$Se_{31.5}$, and CNS-$Se_{30}Te_2$ are shown in Figs. S1–S3 of the Supplemental Material [46], and the estimated lattice parameters for stoichiometric CNS-$Se_{32}$ are ∼11.3038 Å ($a = b = c$) and unit cell volume ($V_c$) ∼ 1444.35 Å$^3$ [52]. Further, the lattice parameters for Se deficient CNS-$Se_{31.5}$ are ∼11.2928 Å ($a = b = c$) and $V_c$ ∼ 1440.14 Å$^3$, whereas for CNS-$Se_{30}Te_2$ are ∼11.3635 Å ($a = b = c$) with a largest $V_c$ ∼ 1467.36 Å$^3$. Figure 1(b) shows the enlarged view of the 222 peak (∼27.3°), where the peak shift with respect to the CNS-$Se_{32}$ sample represents the contraction and expansion of lattice parameters due to the introduction of the Se vacancy in CNS-$Se_{31.5}$ and the heavy Te atom in the CNS-$Se_{30}Te_2$ sample [19,53]. In comparison with the sulfur based colusite, the lattice parameters and corresponding $V_c$ are increased due to the involvement of larger radii Se and Te atoms [38]. The polyhedral cubic crystal structure of CNS-$Se_{32}$ with seven crystallographic sites is shown in Fig. 1(c). Here, the Cu cations have three Wyckoff positions, $Cu_I$ (12$f$), $Cu_{II}$ (8$e$), and $Cu_{III}$ (6$d$), while Nb and Sn cations are present at single sites (2$a$) and (6$c$), respectively. Further, the Se anions have $Se_I$ (24$i$) and $Se_{II}$ (8$e$) Wyckoff positions [54]. The $x$, $y$, and $z$ positions of all the atoms with multiple Wyckoff positions are also shown in Table S1 of the Supplemental Material [46]. All cations like Cu ($Cu_I$, $Cu_{II}$, and $Cu_{III}$), Nb, and Sn are tetrahedrally coordinated with $Se_I$ and $Se_{II}$ anions and form a three dimensional (Cu/Nb/Sn)-$Se_4$ network.

The HR-TEM images in Fig. 2 show that all three samples are crystalline in nature. While the XRD pattern shows the global crystalline nature, TEM images are the local representation of the (200) planes of the crystal structures. Microstructural analysis and the elemental mapping of the constituent elements on the clean and polished surface have been studied using the FE-SEM (Figs. S4–S6 of the Supplemental Material [46]), which confirms the homogeneous distribution of elements and phase purity without any traces of segregation.

## V. RAMAN SPECTROSCOPY AND PHONON CALCULATIONS

CNS-$Se_{32}$ has a cubic ($P\bar{4}3n$ space group) unit cell with 66 atoms ($N$) and thus have a maximum of (3$N$) ∼ 198 phonon modes out of which (3$N$-3) ∼ 195 are optical modes [42,55]. From the group theoretical calculations, the Raman and IR active modes can possibly have $A_1$, $E$, $T_1$, and $T_2$ symmetries where $A_1$ are singly, $E$ are doubly, and $T_1$ and $T_2$ are triply degenerate modes [20,41,55]. Here, we have observed two low frequency $T_1$ (∼55 cm$^{-1}$) and $T_1$ (∼73 cm$^{-1}$) Raman active modes for all the samples [Fig. 3(a)]. The phonon dispersion and the atom-projected density of states (DOS) calculations for CNS-$Se_{32}$ [Figs. 3(b) and 3(c)] show the compressed, flat, and several low frequency optical modes owing to a large number of atoms in the unit cell. Furthermore, the strong acoustic-optical phonon interactions in the region ∼40–55 cm$^{-1}$ leads to more vibrational modes at $X$, $M$, and $R$ symmetry points. These low frequency (ranging 40–80 cm$^{-1}$)

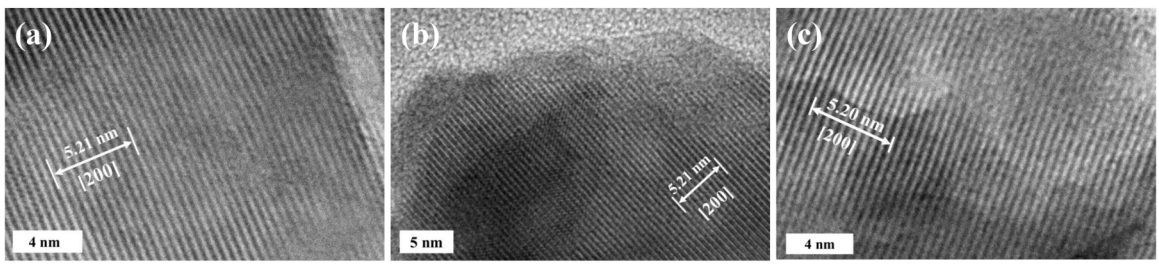


FIG. 2. The bright field HR-TEM images of (a) CNS-$Se_{32}$, (b) CNS-$Se_{31.5}$, and (c) CNS-$Se_{30}Te_2$.

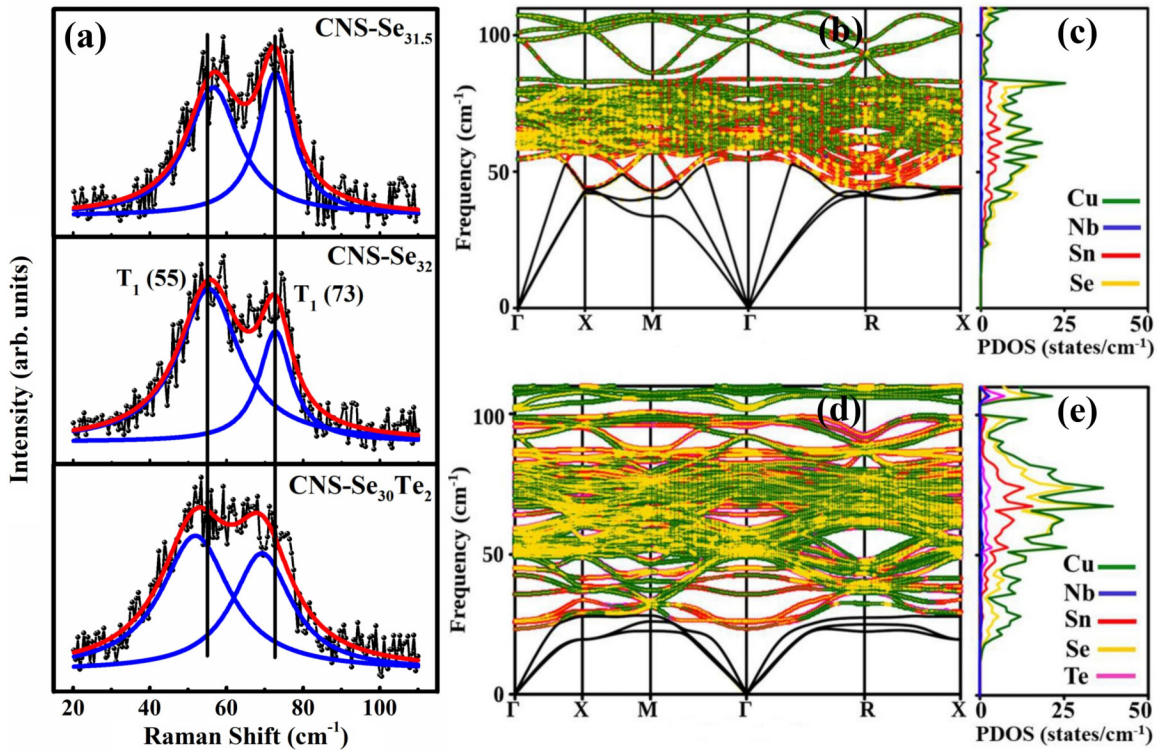


FIG. 3. (a) Room temperature Raman spectra of CNS-$Se_{32}$, CNS-$Se_{31.5}$, and CNS-$Se_{30}Te_2$ in the low frequency region. The black curve represents the experimental data, blue and red curves are the individual and commutative peak fit. (b) The phonon dispersion curve and (c) atom-projected DOS for CNS-$Se_{32}$. (d) The phonon dispersion curve and (e) atom-projected DOS for CNS-$Se_{30}Te_2$.

flat modes are largely due to the mixed vibrations of Cu and Se atoms ($CuSe_4$ tetrahedra). The Cu and Se atoms have multiple Wyck off positions (described as $Cu_I$, $Cu_{II}$, $Cu_{III}$, $Se_I$, and $Se_{II}$) in the crystal lattice of CNS-$Se_{32}$, and the large variation of Cu-Se bond lengths results in inhomogeneous bond strength (Fig. S7 and Table S2 of the Supplemental Material [45]) in $CuSe_4$ tetrahedra. Figure S8 of the Supplemental Material [46] shows the visualization of both the low-lying modes of CNS-$Se_{32}$ which also involves the large contributions of Cu and Se atoms.

The Te involvement results in the lowering of the acoustic phonon cutoff frequency ($\omega_m \sim 30\,\mathrm{cm}^{-1}$), whereas in the case of CNS-$Se_{32}$, the cutoff frequency is $\sim$50 $\mathrm{cm}^{-1}$. The large primitive cell dimensions and the involvement of larger radii Te atoms in the Se site result in enhanced lattice parameters (discussed in the XRD section) and reduced Brillouin zone dimensions, which lower the acoustic phonon $\omega_m$ significantly, since $\omega_m$ is directly related to the size of the first Brillouin zone [44]. Due to the low $\omega_m$, a significant portion of optical phonons occupy the low frequency regions close to the acoustic phonons [Fig. 3(d)]. Furthermore, from the phonon density of states of CNS-$Se_{32}$, the lowest possible optical mode is observed at $\sim$45 $\mathrm{cm}^{-1}$, whereas in CNS-$Se_{30}Te_2$, the lowest possible optical mode is observed at a very low frequency $\sim$25 $\mathrm{cm}^{-1}$. The heavier Te atom is also expected to change the bond strength and results in a significant softening of the optical phonons. A significant softening is observed in both Raman active modes, and can be understood via the relation between the spring constant ($k$), reduced mass ($m$), and characteristic frequency ($\upsilon$) through $\upsilon = \sqrt{\frac{k}{m}}$ [56]. Additionally, from CNS-$Se_{32}$ to CNS-$Se_{30}Te_2$, the acoustic branches show the significant band flatness [Figs. 3(b) and 3(d)] and the increased phonon density of states [Figs. 3(c) and 3(e)] conveying the relatively poor phonon propagation and low $\kappa_l$ in CNS-$Se_{30}Te_2$.

To study the temperature response of Raman active modes, we have performed the temperature dependent Raman measurements (shown in Fig. S9 of the Supplemental Material [46]) and calculated the phonon lifetime ($\tau_i = \frac{1}{2\pi \mathrm{FWHM}_i}$) for the modes from full width at half maximum (FWHM) [57]. The estimated $\tau_i$ is found to be in the range $\sim$0.3–0.7 ps, ultrashort, in the temperature range 300–500 K (Table S3 of the Supplemental Material [46]). The low $\tau_i$ further suggests smaller phonon mean free paths, faster scattering rate, and ultimately hinders the heat carrying phonon transportation inside the solids [57]. Thus, the soft Cu-Se bonding and heavier Te atom affect the vibrational properties and are expected to affect the transport properties as well, significantly.

## VI. ELECTRICAL AND THERMAL TRANSPORT PROPERTIES

Temperature dependent electrical resistivity $\rho(T)$ increases with increasing temperature suggesting the degenerate semiconductorlike nature of charge transport [Fig. 4(a)], which is comparable with the earlier studies of sulfur based colusites [40]. Here, stoichiometric CNS-$Se_{32}$ has the lowest $\rho(T)$ due to the ordered unit cell, whereas CNS-$Se_{30}Te_2$ has the highest $\rho(T)$ because of the presence of Te anions in the Se site. The room temperature Hall carrier densities

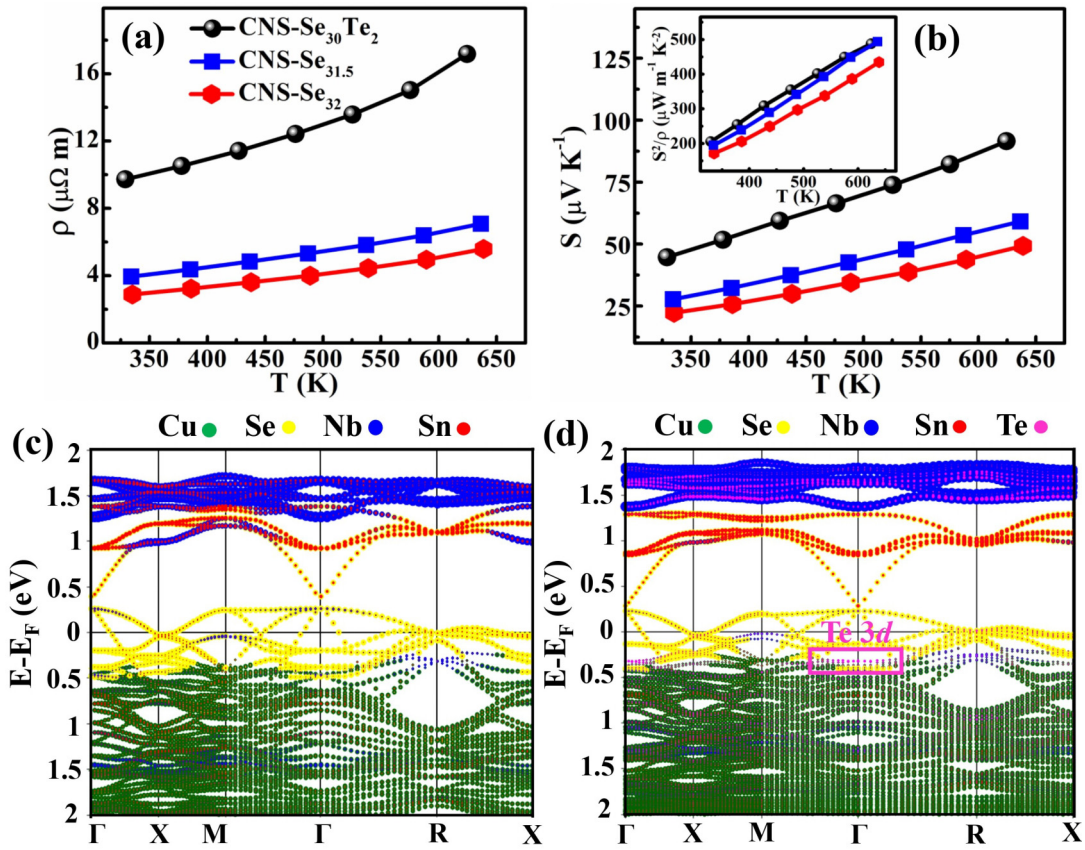


FIG. 4. Temperature dependence of (a) $\rho$, (b) $S$; inset represents the power factor $S^2/\rho$ and electronic band structure of (c) CNS-$Se_{32}$ and (d) CNS-$Se_{30}Te_2$.

are $(n_H) \sim 1.53$, 1.08, and $0.27 \times 10^{21}\,\mathrm{cm}^{-3}$ and mobilities $(\mu_H)$ are ~6.25, 5.37, and $11.80\,\mathrm{cm}^2\,\mathrm{V}^{-1}\,\mathrm{s}^{-1}$ for CNS-$Se_{32}$, CNS-$Se_{31.5}$, and CNS-$Se_{30}Te_2$, respectively. Clearly, the Se vacancies are electron donors which are decreasing the $n_H$ with compensation, while the presence of Te is creating more disorders in the samples. The positive $S(T)$ shows that holes are the majority charge carriers and the CNS-$Se_{30}Te_2$ has the highest $S$ at high temperature [Fig. 4(b)]. Here, the $n_H$ is one order less for CNS-$Se_{30}Te_2$ as compared to CNS-$Se_{32}$, which justifies the high $\rho(T)$ and $S(T)$ in CNS-$Se_{30}Te_2$. Further, CNS-$Se_{31.5}$ and CNS-$Se_{30}Te_2$ have the high $PF$ $(S^2/\rho) \sim 490\,\mu\mathrm{W\,m}^{-1}\,\mathrm{K}^{-2}$, whereas CNS-$Se_{32}$ has $PF \sim 434\,\mu\mathrm{W\,m}^{-1}\,\mathrm{K}^{-2}$ at high temperatures [inset of Fig. 4(b)]. The metallic $\rho(T)$ temperature dependence for all the samples is because of the identical electronic structure near the $E_F$. The unoccupied states above the $E_F$ lead to $p$-type behavior of the compounds. The contribution of various atoms toward the electronic density of states above and below the $E_F$ for CNS-$Se_{32}$ and CNS-$Se_{30}Te_2$ are shown by different colors in Figs. 4(c) and 4(d). In CNS-$Se_{30}Te_2$, the contribution of $3d$ states of Te towards electronic transport results in a change in the total density of states (Fig. S10 of the Supplemental Material [46]), which enhances the $S(T)$.

The temperature dependence of $\kappa_{\mathrm{total}}$ shows a decreasing trend with the rise in temperature [Fig. 5(a)]. Here, the vacancies and the point defects at the anionic sites in CNS-$Se_{31.5}$ offer additional phonon scattering sites leading to a reduction in $\kappa_{\mathrm{total}}$ when compared with CNS-$Se_{32}$. On the other hand, for CNS-$Se_{30}Te_2$, the mass contrast as well as size difference offered by Se and Te atoms due to a difference in the atomic radii [~190 pm (Se) and ~210 pm (Te)] enhances the phonon scattering leading to a large reduction in the $\kappa_{\mathrm{total}}$. The plots of $D$ and $\kappa_e$ are presented in Figs. S11 and S12 of the Supplemental Material [46]. The relatively low $\rho(T)$ values for the CNS-$Se_{32}$ and CNS-$Se_{31.5}$ result in larger $\kappa_e$ values than CNS-$Se_{30}Te_2$. Furthermore, the lattice contribution $\kappa_l$ shows $1/T$ dependence due to anharmonic umklapp processes [Fig. 5(b)] [58]. At high temperature (~625 K), CNS-$Se_{30}Te_2$ has the relatively lowest $\kappa_l \sim 0.76\,\mathrm{W\,m}^{-1}\,\mathrm{K}^{-1}$ due to high disorder, resulting in a TE figure of merit ~0.21, which is three times larger than stoichiometric CNS-$Se_{32}$. To understand better the inherent poor $\kappa_{\mathrm{total}}$, we have analyzed the low temperature heat capacity data and extract the possible interactions of acoustic and optical phonons.

## VII. HEAT CAPACITY

The temperature dependence of $C_p$ at low temperature is shown in Figs. 6(a)–6(c). The anomalous negative value of the electronic term $(\gamma)$ in fitting with the Debye model indicates that the $C_p$ analysis cannot be examined from a single Debye mode [59]. Therefore, we have fitted the data using one Debye-three Einstein ($1D$-$3E$) mode model using

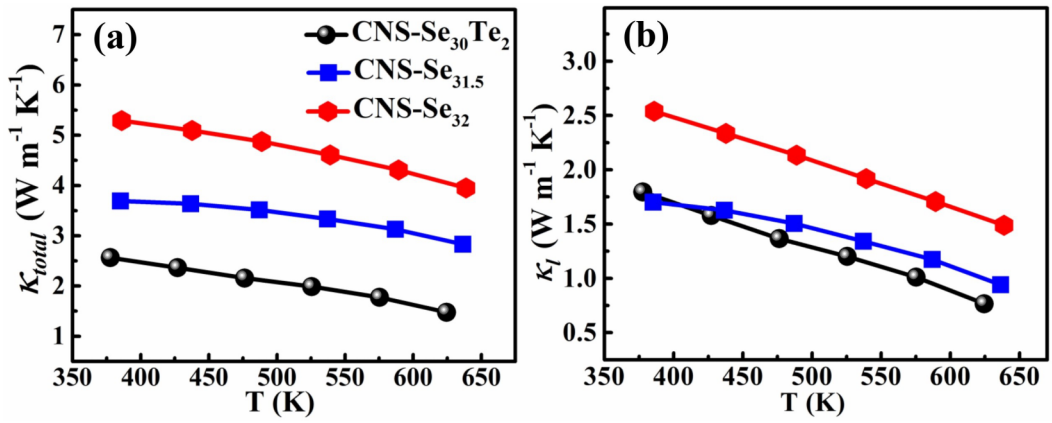


FIG. 5. Temperature dependence of (a) $\kappa_{\text{total}}$ and (b) $\kappa_l$.

the following equation:

$$\frac{C_p}{T} = \gamma + \beta T^2 + A\Theta_{E1}^2 T^{2^{(-3/2)}} \frac{e^{\Theta_{E1}/T}}{(e^{\Theta_{E1}/T}-1)^2} + B\Theta_{E2}^2 T^{2^{(-3/2)}} \frac{e^{\Theta_{E2}/T}}{(e^{\Theta_{E2}/T}-1)^2} + C\Theta_{E3}^2 T^{2^{(-3/2)}} \times \frac{e^{\Theta_{E3}/T}}{(e^{\Theta_{E3}/T}-1)^2},$$

where $\gamma$ and $\beta$ represents the electronic and lattice contribution of heat capacity; $A$, $B$, and $C$ are the material constants, and $\Theta_{E1}$, $\Theta_{E2}$, and $\Theta_{E3}$ are the three Einstein temperatures [60]. The large $\gamma$ may be due to the large electronic density of states near the $E_F$ and due to the contribution of other factors (except the linear term) as discussed in earlier reports [31,61,62]. The obtained $\Theta_E$ for CNS-$Se_{32}$ are ~23.11 K (16.06 $cm^{-1}$), ~54.64 K (37.98 $cm^{-1}$), and ~95.55 (66.41 $cm^{-1}$) as shown in Table S4 of the Supplemental Material [46]. The $\Theta_{E1}$, $\Theta_{E2}$, and $\Theta_{E3}$ individually contribute to

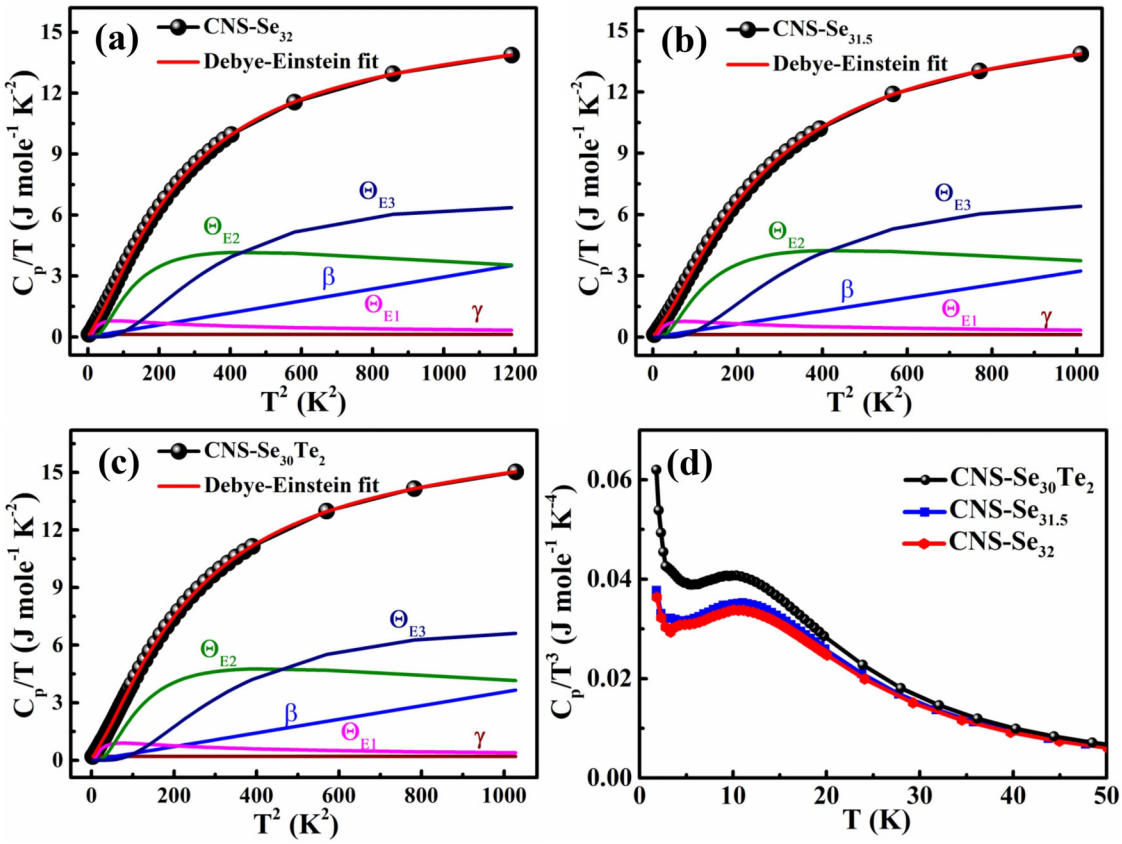


FIG. 6. Temperature dependence of heat capacity fitted with one Debye and three Einstein modes for (a) CNS-$Se_{32}$, (b) CNS-$Se_{31.5}$, (c) CNS-$Se_{30}Te_2$, and (d) $C_p/T^3$ vs $T$ plot.

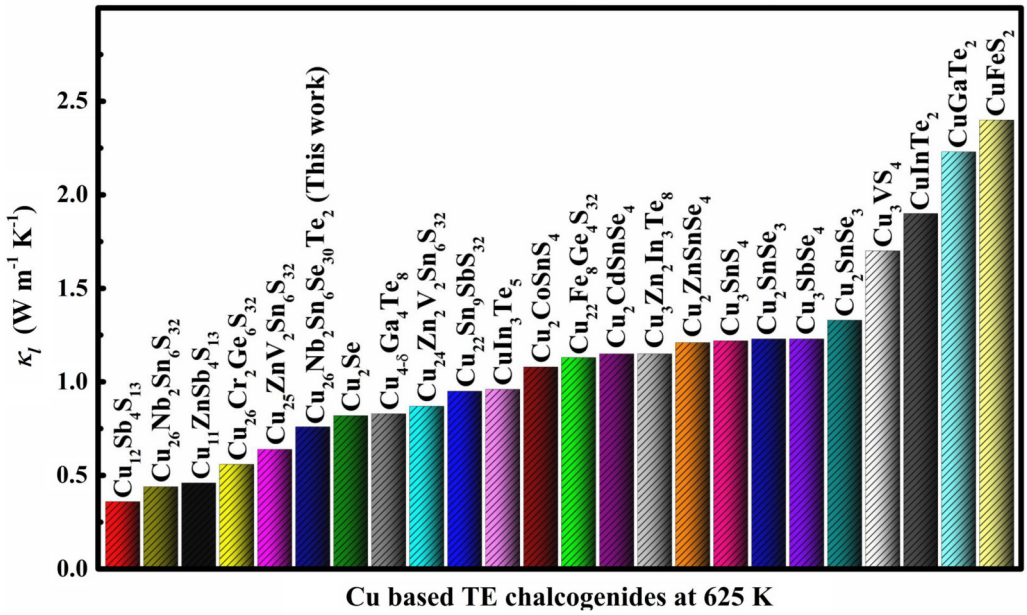


FIG. 7. Comparison of the $\kappa_l$ of CNS-$Se_{30}Te_2$ sample with other copper-based chalcogenide materials at 625 K [17,19,24,25,32,37,40,45,70–81].

the total $C_p/T$ where, $\Theta_{E1}$ dominates below ~7 K, $\Theta_{E2}$ from ~7 to 23 K, and $\Theta_{E3}$ above ~23 K. The energy of the Einstein mode is equivalent to the observed low frequency Raman active modes $T_1$ (~55 cm$^{-1}$) and $T_1$ (~73 cm$^{-1}$), and thus the interactions of these modes provide extra phonon scattering in these samples.

The Debye temperature and average sound velocity are estimated from the heat capacity fitting data and shown in Table S4 of the Supplemental Material [46]. From CNS-$Se_{32}$ to CNS-$Se_{30}Te_2$, the $\kappa_l$ decreases as the Debye temperature and average sound velocity of these materials decrease. Further, the presence of localized Einstein modes, strong acoustic and optical phonon scattering, low average sound velocity, and excess vibrational density of states at low temperature strongly affect the $\kappa_l$ of the materials [20]. Thus, the interaction of low energy phonons results in poor thermal transport and $\kappa_l$. The excess vibrational DOS at low temperature leads to the deviation in Debye $T^3$ law which is a universal feature in the system having glasslike thermal properties and the peak is called a "boson peak" (BP) as shown in Fig. 6(d) [63,64]. For this non-Debye behavior the acoustic and phonon interaction plays a very crucial role which is associated with soft/loosely bonded Cu atoms [63–66]. From stoichiometric CNS-$Se_{32}$ to alloy CNS-$Se_{30}Te_2$, the addition of Te atoms in Se sites results in a significant increase in $C_p/T^3$ which might be due to the increased electronic contribution ($\gamma$) and phononic density of states in CNS-$Se_{30}Te_2$ [63].

Beside these factors, the low $\kappa_l$ can also be understood by the crystal anharmonicity which is governed by the Grüneisen parameter ($\gamma_G$) which relates to the crystal volume and phonon frequency [10]. The large crystal anharmonicity in the compound causes large damping effects and enhances the phonons scattering. We calculated the $\gamma_G$ from $\gamma_G = ((3.1 \times 10^{-6})\frac{M_a \delta \Theta_D^3}{\kappa_l N^{2/3} T})^{1/2}$, where $M_a$ is the average atomic mass in amu, $\delta^3$ is the atomic volume (volume per unit), $\Theta_D$ is the Debye temperature, $\gamma_G$ is the Gruneisen parameter, $N$ is the total number of atoms present in the primitive unit cell, and $T$ is the temperature [67]. We obtained $\gamma_G \sim 1.46$, 1.77, and 1.98, for CNS-$Se_{32}$, CNS-$Se_{31.5}$, and CNS-$Se_{30}Te_2$, respectively, and the values are higher than many state-of-the-art TE materials like $Bi_2Te_3$, $Sb_2Te_3$, PbTe, PbSe, and PbS [68]. The significantly enhanced $\gamma_G$ in CNS-$Se_{30}Te_2$ compared to that in CNS-$Se_{32}$ is due to the presence of disorder and mass difference at anionic site as both anions (Se and Te) are present at the same site (24*i* and 8*e*) and due to the change in crystal volume [69]. The phonon dynamics of these large unit cell materials can also be investigated for their crystal anharmonicity and low $\kappa_l$ through inelastic neutron scattering, Mössbauer spectroscopy, and more advanced calculations [14,28,35]. These techniques further provide insightful information about the structural information, chemical environment of soft-bonded Cu-atoms, and localized vibrational motions of atoms, which overall affects the thermal properties of the materials [13,14,28,35].

A comparative study of $\kappa_l$ of CNS-$Se_{30}Te_2$ with different Cu-based binary, ternary, and quaternary chalcogenides is shown in Fig. 7. The value of $\kappa_l$, lower than most Cu based TE chalcogenides, can be understood due to the relatively large Grüneisen parameter, soft-bonded Cu-Se crystal framework, and softening of Raman active modes in CNS-$Se_{30}Te_2$ in comparison to CNS-$Se_{32}$, CNS-$Se_{31.5}$, and the above shown compounds. The $\kappa_l$ values in these mixed chalcogen series of materials can further be lowered through more optimized alloying or substitutions. In the case of tetrahedrites and colusites, the Cu atom contributes significantly at low energy, and the anharmonic rattling motion and structural disorder altogether enhance the phonon scattering and thus have lower $\kappa_l$ [9,14,20,82]. Overall, the interaction of low energy acoustic

and optical phonons results in poor thermal transport which can be effective for future applications.

## VIII. CONCLUSION

In summary, the scattering of acoustic and optical phonons in Se based synthetic minerals is accountable for inherently poor $\kappa_l$. The Grüneisen parameter in CNS-$Se_{30}Te_2$ suggests strong crystal anharmonicity leading to low $\kappa_l \sim 0.76\,W\,m^{-1}\,K^{-1}$ at $\sim 625\,K$, where the structural disorder induced by the Te atom enhances the phonon scattering. The Te in the Se sites reduces the $\kappa_l$ largely through the lowering of acoustic phonon cutoff frequency, flattening the heat carried phonon branches and softening the optical modes. The excess vibrational density of states results in the appearance of a Boson peak due to deviation in the Debye $T^3$ law. The low frequency Raman and Einstein modes are mainly associated with soft-bonded Cu-Se tetrahedra. Additionally, the phonon lifetime $\sim$1 ps confirms the high scattering rate causing low thermal conductivity in these compounds. Overall, our results provide a comprehensive way to study the inherent low $\kappa_l$ in large unit cell crystalline materials.

## ACKNOWLEDGMENTS

A.S. acknowledges DST-SERB India (Grant No. CRG/2018/002197) for funding support and IIT Mandi for research facilities.

[1] D. M. Rowe, *CRC Handbook of Thermoelectrics* (CRC, Boca Raton, FL, 1995).

[2] L.-D. Zhao, S. Hao, S.-H. Lo, C.-I. Wu, X. Zhou, Y. Lee, H. Li, K. Biswas, T. P. Hogan, C. Uher *et al.*, High thermoelectric performance via hierarchical compositionally alloyed nanostructures, J. Am. Chem. Soc. **135**, 7364 (2013).

[3] K. Biswas, J. He, I. D. Blum, C.-I. Wu, T. P. Hogan, D. N. Seidman, V. P. Dravid, and M. G. Kanatzidis, High-performance bulk thermoelectrics with all-scale hierarchical architectures, Nature (London) **489**, 414 (2012).

[4] S. Acharya, J. Pandey, and A. Soni, Soft phonon modes driven reduced thermal conductivity in self-compensated $Sn_{1.03}Te$ with Mn doping, Appl. Phys. Lett. **109**, 133904 (2016).

[5] S. Bathula, M. Jayasimhadri, B. Gahtori, N. K. Singh, K. Tyagi, A. K. Srivastava, and A. Dhar, The role of nanoscale defect features in enhancing the thermoelectric performance of p-type nanostructured SiGe alloys, Nanoscale **7**, 12474 (2015).

[6] M. K. Jana, K. Pal, A. Warankar, P. Mandal, U. V. Waghmare, and K. Biswas, Intrinsic rattler-induced low thermal conductivity in zintl type $TlInTe_2$, J. Am. Chem. Soc. **139**, 4350 (2017).

[7] T. Takabatake, K. Suekuni, T. Nakayama, and E. Kaneshita, Phonon-glass electron-crystal thermoelectric clathrates: Experiments and theory, Rev. Mod. Phys. **86**, 669 (2014).

[8] S. Acharya, J. Pandey, and A. Soni, Enhancement of power factor for inherently poor thermal conductor $Ag_8GeSe_6$ by replacing Ge with Sn, ACS Appl. Energy Mater. **2**, 654 (2019).

[9] K. S. Rana and A. Soni, Thermoelectricity in Ag/Cu-based complex crystal structure minerals with inherent low thermal conductivity, Oxford Open Mater. Sci. **3**, itad005 (2023).

[10] N. K. Singh and A. Soni, Crystalline anharmonicity and ultralow thermal conductivity in layered $Bi_2GeTe_4$ for thermoelectric applications, Appl. Phys. Lett. **117**, 123901 (2020).

[11] P. Acharyya, T. Ghosh, K. Pal, K. Kundu, K. Singh Rana, J. Pandey, A. Soni, U. V. Waghmare, and K. Biswas, Intrinsically ultralow thermal conductivity in ruddlesden–popper 2D perovskite $Cs_2PbI_2Cl_2$: Localized anharmonic vibrations and dynamic octahedral distortions, J. Am. Chem. Soc. **142**, 15595 (2020).

[12] M. S. Kushwaha, P. Halevi, L. Dobrzynski, and B. Djafari-Rouhani, Acoustic Band Structure of Periodic Elastic Composites, Phys. Rev. Lett. **71**, 2022 (1993).

[13] Y. Bouyrie, C. Candolfi, S. Pailhès, M. M. Koza, B. Malaman, A. Dauscher, J. Tobola, O. Boisron, L. Saviot, and B. Lenoir, From crystal to glass-like thermal conductivity in crystalline minerals, Phys. Chem. Chem. Phys. **17**, 19751 (2015).

[14] W. Lai, Y. Wang, D. T. Morelli, and X. Lu, From bonding asymmetry to anharmonic rattling in $Cu_{12}Sb_4S_{13}$ tetrahedrites: When lone-pair electrons are not so lonely, Adv. Funct. Mater. **25**, 3648 (2015).

[15] G. Guélou, P. Lemoine, B. Raveau, and E. Guilmeau, Recent developments in high-performance thermoelectric sulphides: An overview of the promising synthetic colusites, J. Mater. Chem. C **9**, 773 (2021).

[16] K. Suekuni and T. Takabatake, Cu–S based synthetic minerals as efficient thermoelectric materials at medium temperatures, APL Mater. **4**, 104503 (2016).

[17] P. Qiu, X. Shi, and L. Chen, Cu-based thermoelectric materials, Energy Storage Mater. **3**, 85 (2016).

[18] D. Rawat, A. Singh, N. K. Singh, and A. Soni, Anisotropic light-matter interactions in the single-crystal topological insulator bismuth selenide, Phys. Rev. B **107**, 155203 (2023).

[19] K. Suekuni, F. S. Kim, H. Nishiate, M. Ohta, H. I. Tanaka, and T. Takabatake, High-performance thermoelectric minerals: Colusites $Cu_{26}V_2M_6S_{32}$ (M = Ge, Sn), Appl. Phys. Lett. **105**, 132107 (2014).

[20] C. Bourgès, Y. Bouyrie, A. R. Supka, R. Al Rahal Al Orabi, P. Lemoine, O. I. Lebedev, M. Ohta, K. Suekuni, V. Nassif, V. Hardy *et al.*, High-performance thermoelectric bulk colusite by process controlled structural disordering, J. Am. Chem. Soc. **140**, 2186 (2018).

[21] G. Guélou, C. Couder, A. Bourhim, O. I. Lebedev, N. Daneu, F. Appert, J. Juraszek, P. Lemoine, L. Segreto, and E. Guilmeau, A scalable synthesis route for multiscale defect engineering in the sustainable thermoelectric quaternary sulfide $Cu_{26}V_2Sn_6S_{32}$, Acta Mater. **195**, 229 (2020).

[22] G. Guélou, V. Pavan Kumar, A. Bourhim, P. Lemoine, B. Raveau, A. Supka, O. I. Lebedev, R. Al Rahal Al Orabi, M. Fornari, K. Suekuni *et al.*, Toppling the transport properties with cationic overstoichiometry in thermoelectric colusite: $[Cu_{26}Cr_2Ge_6]_{1+\delta}S_{32}$, ACS Appl. Energy Mater. **3**, 4180 (2020).

[23] Y. Shimizu, K. Suekuni, H. Saito, P. Lemoine, E. Guilmeau, B. Raveau, R. Chetty, M. Ohta, T. Takabatake, and M. Ohtaki, Synergistic effect of chemical substitution and insertion on the

thermoelectric performance of $Cu_{26}V_2Ge_6S_{32}$ colusite, Inorg. Chem. **60**, 11364 (2021).

[24] T. Plirdpring, K. Kurosaki, A. Kosuga, T. Day, S. Firdosy, V. Ravi, G. J. Snyder, A. Harnwunggmoung, T. Sugahara, Y. Ohishi *et al.*, Chalcopyrite $CuGaTe_2$: A high-efficiency bulk thermoelectric material, Adv. Mater. **24**, 3622 (2012).

[25] X. Lu, D. T. Morelli, Y. Xia, F. Zhou, V. Ozolins, H. Chi, X. Zhou, and C. Uher, High performance thermoelectricity in earth-abundant compounds based on natural mineral tetrahedrites, Adv. Energy Mater. **3**, 342 (2013).

[26] T. Nakada, M. Takahashi, C. Shijimaya, K. Higashimine, W. Zhou, P. Dwivedi, M. Ohta, H. Takida, T. Akatsuka, M. Miyata *et al.*, Gram-scale synthesis of tetrahedrite nanoparticles and their thermoelectric properties, Langmuir **35**, 16335 (2019).

[27] Y. Bouyrie, C. Candolfi, A. Dauscher, B. Malaman, and B. Lenoir, Exsolution process as a route toward extremely low thermal conductivity in $Cu_{12}Sb_{4-x}Te_xS_{13}$ tetrahedrites, Chem. Mater. **27**, 8354 (2015).

[28] K. Suekuni, C. H. Lee, H. I. Tanaka, E. Nishibori, A. Nakamura, H. Kasai, H. Mori, H. Usui, M. Ochi, T. Hasegawa *et al.*, Retreat from stress: Rattling in a planar coordination, Adv. Mater. **30**, 1706230 (2018).

[29] S. Lin, W. Li, and Y. Pei, Thermally insulative thermoelectric argyrodites, Mater. Today **48**, 198 (2021).

[30] J. L. Niedziela, D. Bansal, A. F. May, J. Ding, T. Lanigan-Atkins, G. Ehlers, D. L. Abernathy, A. Said, and O. Delaire, Selective breakdown of phonon quasiparticles across superionic transition in $CuCrSe_2$, Nat. Phys. **15**, 73 (2019).

[31] P. Qiu, T. Zhang, Y. Qiu, X. Shi, and L. Chen, Sulfide bornite thermoelectric material: A natural mineral with ultralow thermal conductivity, Energy Environ. Sci. **7**, 4000 (2014).

[32] Y. Yang, P. Ying, J. Wang, X. Liu, Z. Du, Y. Chao, and J. Cui, Enhancing the thermoelectric performance of $Cu_3SnS_4$-based solid solutions through coordination of the Seebeck coefficient and carrier concentration, J. Mater. Chem. A **5**, 18808 (2017).

[33] J. M. Skelton, A. J. Jackson, M. Dimitrievska, S. K. Wallace, and A. Walsh, Vibrational spectra and lattice thermal conductivity of kesterite-structured $Cu_2ZnSnS_4$ and $Cu_2ZnSnSe_4$, APL Mater. **3**, 041102 (2015).

[34] C. Sevik and T. Çağın, Assessment of thermoelectric performance of $Cu_2ZnSnX_4$, $X$ = S, Se, and Te, Appl. Phys. Lett. **95**, 112105 (2009).

[35] C. Candolfi, G. Guélou, C. Bourgès, A. R. Supka, R. Al Rahal Al Orabi, M. Fornari, B. Malaman, G. Le Caër, P. Lemoine, V. Hardy *et al.*, Disorder-driven glasslike thermal conductivity in colusite $Cu_{26}V_2Sn_6S_{32}$ investigated by Mössbauer spectroscopy and inelastic neutron scattering, Phys. Rev. Mater. **4**, 025404 (2020).

[36] S. O. Long, A. V. Powell, S. Hull, F. Orlandi, C. C. Tang, A. R. Supka, M. Fornari, and P. Vaqueiro, Jahn-teller driven electronic instability in thermoelectric tetrahedrite, Adv. Funct. Mater. **30**, 1909409 (2020).

[37] P. Ventrapati, G. Guélou, P. Lemoine, B. Raveau, A. Supka, R. Al Rahal Al Orabi, M. Fornari, and K. Suekuni, Copper-rich thermoelectric sulfides: Size mismatch effect and chemical disorder in the $[TS_4]Cu_6$ complexes of $Cu_{26}T_2Ge_6S_{32}$ (T = Cr, Mo, W) colusites, Angew. Chem. Int. Ed. **58**, 15455 (2019).

[38] Y. Bouyrie, M. Ohta, K. Suekuni, Y. Kikuchi, P. Jood, A. Yamamoto, and T. Takabatake, Enhancement in the thermoelectric performance of colusites $Cu_{26}A_2E_6S_{32}$ (A = Nb, Ta; E = Sn, Ge) using E-site non-stoichiometry, J. Mater. Chem. C **5**, 4174 (2017).

[39] F. S. Kim, K. Suekuni, H. Nishiate, M. Ohta, H. I. Tanaka, and T. Takabatake, Tuning the charge carrier density in the thermoelectric colusite, J. Appl. Phys. **119**, 175105 (2016).

[40] Y. Kikuchi, Y. Bouyrie, M. Ohta, K. Suekuni, M. Aihara, and T. Takabatake, Vanadium-free colusites $Cu_{26}A_2Sn_6S_{32}$ (A = Nb, Ta) for environmentally friendly thermoelectrics, J. Mater. Chem. A **4**, 15207 (2016).

[41] V. Pavan Kumar, A. R. Supka, P. Lemoine, O. I. Lebedev, B. Raveau, K. Suekuni, V. Nassif, R. Al Rahal Al Orabi, M. Fornari, and E. Guilmeau, High power factors of thermoelectric colusites $Cu_{26}T_2Ge_6S_{32}$ (T = Cr, Mo, W): Toward functionalization of the conductive "Cu–S" network, Adv. Energy Mater. **9**, 1803249 (2019).

[42] K. Suekuni, Y. Shimizu, E. Nishibori, H. Kasai, H. Saito, D. Yoshimoto, K. Hashikuni, Y. Bouyrie, R. Chetty, M. Ohta *et al.*, Atomic-scale phonon scatterers in thermoelectric colusites with a tetrahedral framework structure, J. Mater. Chem. A **7**, 228 (2019).

[43] R. Gupta and C. Bera, High thermoelectric figure of merit predicted in $Cu_{26}V_2Sn_6Se_{32}$ colusite induced by vacancy defects and glassy-like vibrational modes, J. Appl. Phys. **130**, 065106 (2021).

[44] Z. Chen, X. Zhang, and Y. Pei, Manipulation of phonon transport in thermoelectrics, Adv. Mater. **30**, 1705617 (2018).

[45] P. Kamińska, C. Bourgès, R. Chetty, D. Gutiérrez-Del-Río, P. Śpiewak, W. Święszkowski, T. Nishimura, and T. Mori, Insight into the preponderant role of the lattice size in Sn-based colusites for promoting a high power factor, J. Mater. Chem. A **10**, 10701 (2022).

[46] See Supplemental Material at http://link.aps.org/supplemental/10.1103/PhysRevB.108.045202 for Rietveld, Raman, and thermal transport analysis.

[47] P. E. Blöchl, Projector augmented-wave method, Phys. Rev. B **50**, 17953 (1994).

[48] G. Kresse and J. Furthmüller, Efficient iterative schemes for ab initio total-energy calculations using a plane-wave basis set, Phys. Rev. B **54**, 11169 (1996).

[49] G. Kresse and D. Joubert, From ultrasoft pseudopotentials to the projector augmented-wave method, Phys. Rev. B **59**, 1758 (1999).

[50] J. P. Perdew, K. Burke, and M. Ernzerhof, Generalized Gradient Approximation Made Simple, Phys. Rev. Lett. **77**, 3865 (1996).

[51] A. Togo and I. Tanaka, First principles phonon calculations in materials science, Scr. Mater. **108**, 1 (2015).

[52] J. Rodríguez-Carvajal, Recent advances in magnetic structure determination by neutron powder diffraction, Phys. B (Amsterdam, Neth.) **192**, 55 (1993).

[53] S. Wang, W. Xie, H. Li, and X. Tang, Enhanced performances of melt spun $Bi_2(Te, Se)_3$ for n-type thermoelectric legs, Intermetallics **19**, 1024 (2011).

[54] O. Frank-Kamenetskaya, I. Rozhdestvenskaya, and L. Yanulova, New data on the crystal structures of colusites and arsenosulvanites, J. Struct. Chem. **43**, 89 (2002).

[55] T. Hagiwara, K. Suekuni, P. Lemoine, A. R. Supka, R. Chetty, E. Guilmeau, B. Raveau, M. Fornari, M. Ohta, R. Al Rahal Al Orabi *et al.*, Key role of $d^0$ and $d^{10}$ cations for the design of semiconducting colusites: Large thermoelectric ZT in $Cu_{26}Ti_2Sb_6S_{32}$ compounds, Chem. Mater. **33**, 3449 (2021).

[56] K. Dovstam, Simulation of damped vibrations based on augmented Hooke's law and elastic modes of vibration, Int. J. Solids Struct. **37**, 5413 (2000).

[57] J. Pandey, S. Mukherjee, D. Rawat, S. Athar, K. S. Rana, R. C. Mallik, and A. Soni, Raman spectroscopy study of phonon liquid electron crystal in copper deficient superionic thermoelectric $Cu_{2-x}Te$, ACS Appl. Energy Mater. **3**, 2175 (2020).

[58] B. Abeles, Lattice thermal conductivity of disordered semiconductor alloys at high temperatures, Phys. Rev. **131**, 1906 (1963).

[59] A. Sussardi, T. Tanaka, A. U. Khan, L. Schlapbach, and T. Mori, Enhanced thermoelectric properties of samarium boride, J. Materiomics **1**, 196 (2015).

[60] I. K. Dimitrov, M. E. Manley, S. M. Shapiro, J. Yang, W. Zhang, L. D. Chen, Q. Jie, G. Ehlers, A. Podlesnyak, J. Camacho *et al.*, Einstein modes in the phonon density of states of the single-filled skutterudite $Yb_{0.2}Co_4Sb_{12}$, Phys. Rev. B **82**, 174301 (2010).

[61] H. Xie, S. Hao, J. Bao, T. J. Slade, G. J. Snyder, C. Wolverton, and M. G. Kanatzidis, All-inorganic halide perovskites as potential thermoelectric materials: Dynamic cation off-centering induces ultralow thermal conductivity, J. Am. Chem. Soc. **142**, 9553 (2020).

[62] R. Gumeniuk, M. Schöneich, A. Leithe-Jasper, W. Schnelle, M. Nicklas, H. Rosner, A. Ormeci, U. Burkhardt, M. Schmidt, U. Schwarz *et al.*, High-pressure synthesis and exotic heavy-fermion behaviour of the filled skutterudite $SmPt_4Ge_{12}$, New J. Phys. **12**, 103035 (2010).

[63] S. Kojima, Y. Matsuda, M. Kodama, H. Kawaji, and T. Atake, Boson peaks and excess heat capacity of lithium borate glasses, Chin. J. Phys. Taipei **49**, 414 (2011).

[64] S. Kojima and H. Kawaji, Low-temperature excess heat capacity and boson peak of mixed alkali effect in borate glass, Thermochim. Acta **669**, 156 (2018).

[65] P. Lunkenheimer and A. Loidl, High-frequency excitations in glassy crystals, J. Non-Cryst. Solids **352**, 4556 (2006).

[66] S. Acharya, S. Anwar, T. Mori, and A. Soni, Coupling of charge carriers with magnetic entropy for power factor enhancement in Mn doped $Sn_{1.03}Te$ for thermoelectric applications, J. Mater. Chem. C **6**, 6489 (2018).

[67] Y. Xiao, C. Chang, Y. Pei, D. Wu, K. Peng, X. Zhou, S. Gong, J. He, Y. Zhang, Z. Zeng *et al.*, Origin of low thermal conductivity in SnSe, Phys. Rev. B **94**, 125203 (2016).

[68] T. Jia, G. Chen, and Y. Zhang, Lattice thermal conductivity evaluated using elastic properties, Phys. Rev. B **95**, 155206 (2017).

[69] M. Dutta, K. Pal, U. V. Waghmare, and K. Biswas, Bonding heterogeneity and lone pair induced anharmonicity resulted in ultralow thermal conductivity and promising thermoelectric properties in n-type $AgPbBiSe_3$, Chem. Sci. **10**, 4905 (2019).

[70] V. Pavan Kumar, P. Lemoine, V. Carnevali, G. Guélou, O. I. Lebedev, P. Boullay, B. Raveau, R. Al Rahal Al Orabi, M. Fornari, C. Prestipino *et al.*, Ordered sphalerite derivative $Cu_5Sn_2S_7$: A degenerate semiconductor with high carrier mobility in the Cu–Sn–S diagram, J. Mater. Chem. A **9**, 10812 (2021).

[71] H. Xie, X. Su, G. Zheng, T. Zhu, K. Yin, Y. Yan, C. Uher, M. G. Kanatzidis, and X. Tang, The Role of Zn in chalcopyrite $CuFeS_2$: Enhanced thermoelectric properties of $Cu_{1-x}Zn_xFeS_2$ with In situ nanoprecipitates, Adv. Energy Mater. **7**, 1601299 (2017).

[72] W. Li, S. Lin, X. Zhang, Z. Chen, X. Xu, and Y. Pei, Thermoelectric Properties of $Cu_2SnSe_4$ with intrinsic vacancy, Chem. Mater. **28**, 6227 (2016).

[73] Q. Zhang, L. Xi, J. Zhang, C. Wang, L. You, S. Pan, K. Guo, Z. Li, and J. Luo, Influence of Ag substitution on thermoelectric properties of the quaternary diamond-like compound $Zn_2Cu_3In_3Te_8$, J. Materiomics **7**, 236 (2020).

[74] D. Zhang, J. Yang, Q. Jiang, Z. Zhou, X. Li, J. Xin, A. Basit, Y. Ren, and X. He, Multi-cations compound $Cu_2CoSnS_4$: DFT calculating, band engineering and thermoelectric performance regulation, Nano Energy **36**, 156 (2017).

[75] Y. Lu, S. Chen, W. Wu, Z. Du, Y. Chao, and J. Cui, Enhanced thermoelectric performance of a chalcopyrite compound $CuIn_3Se_{5-x}Te_x$ ($x = 0{\sim}0.5$) through crystal structure engineering, Sci. Rep. **7**, 40224 (2017).

[76] J. Cui, J. Zhu, Z. Han, and Y. Luo, Significantly improved thermal stability and thermoelectric performance of Cu-deficient $Cu_{4-\delta}Ga_4Te_8$ ($\delta = 1.12$) chalcogenides through addition of Sb, J. Mater. Chem. A **6**, 12672 (2018).

[77] S. Ballikaya, H. Chi, J. R. Salvador, and C. Uher, Thermoelectric properties of Ag-doped $Cu_2Se$ and $Cu_2Te$, J. Mater. Chem. A **1**, 12478 (2013).

[78] V. P. Kumar, P. Lemoine, V. Carnevali, G. Guélou, O. I. Lebedev, B. Raveau, R. Al Rahal Al Orabi, M. Fornari, C. Candolfi, C. Prestipino *et al.*, Local-disorder-induced low thermal conductivity in degenerate semiconductor $Cu_{22}Sn_{10}S_{32}$, Inorg. Chem. **60**, 16273 (2021).

[79] L. Paradis Fortin, G. Guélou, P. Ventrapati, P. Lemoine, C. Prestipino, O. Merdrignac-Conanec, G. R. Durand, S. Cordier, and O. Lebedev, Structure, microstructure and thermoelectric properties of germanite-type $Cu_{22}Fe_8Ge_4S_{32}$ compounds, J. Alloys Compd. **831**, 154767 (2020).

[80] T. Deng, T. Xing, M. K. Brod, Y. Sheng, P. Qiu, I. Veremchuk, Q. Song, T.-R. Wei, J. Yang, G. J. Snyder *et al.*, Discovery of high-performance thermoelectric copper chalcogenide using modified diffusion-couple high-throughput synthesis and automated histogram analysis technique, Energy Environ. Sci. **13**, 3041 (2020).

[81] C. Bourgès, M. Gilmas, P. Lemoine, N. E. Mordvinova, O. I. Lebedev, E. Hug, V. Nassif, B. Malaman, R. Daou, and E. Guilmeau, Structural analysis and thermoelectric properties of mechanically alloyed colusites, J. Mater. Chem. C **4**, 7455 (2016).

[82] A. V. Powell, Recent developments in Earth-abundant copper-sulfide thermoelectric materials, J. Appl. Phys. **126**, 100901 (2019).